APPLIED SCIENCES AND ENGINEERING

3D printed patient-specific aortic root models with internal sensors for minimally invasive applications

Ghazaleh Haghiashtiani[1]*, Kaiyan Qiu[1]*, Jorge D. Zhingre Sanchez[2,3], Zachary J. Fuenning[1], Priya Nair[4], Sarah E. Ahlberg[4], Paul A. Iaizzo[2,3,5], Michael C. McAlpine[1,5†]

Minimally invasive surgeries have numerous advantages, yet complications may arise from limited knowledge about the anatomical site targeted for the delivery of therapy. Transcatheter aortic valve replacement (TAVR) is a minimally invasive procedure for treating aortic stenosis. Here, we demonstrate multimaterial three-dimensional printing of patient-specific soft aortic root models with internally integrated electronic sensor arrays that can augment testing for TAVR preprocedural planning. We evaluated the efficacies of the models by comparing their geometric fidelities with postoperative data from patients, as well as their in vitro hemodynamic performances in cases with and without leaflet calcifications. Furthermore, we demonstrated that internal sensor arrays can facilitate the optimization of bioprosthetic valve selections and in vitro placements via mapping of the pressures applied on the critical regions of the aortic anatomies. These models may pave exciting avenues for mitigating the risks of postoperative complications and facilitating the development of next-generation medical devices.

INTRODUCTION

In the coming decades, the world will face a shift in demographics and an aging population. It has been estimated that by the year 2030, the number of adults over the age of 65 years in the United States alone will reach 73.1 million, comprising 21% of its total population (*1*). An aging population increases the prevalence of cardiovascular diseases, which are leading causes of death in this age group (*2*). Noncongenital aortic stenosis (AS) is one of the common cardiovascular conditions in the elderly that affects about 2.7 million adults over the age of 75 in North America (*3*). AS is associated with the narrowing of the aortic valve orifice area due to calcification that impedes the leaflets' full range of motion, causing obstruction to blood flow from the left ventricle to the aorta and, ultimately, ventricular dysfunction (*4*). Given the age of individuals suffering from AS and the prevalence of comorbidities in this population, some patients are deemed high risk for surgical valve replacement via open heart surgery (*4*, *5*). Transcatheter aortic valve replacement (TAVR) is a minimally invasive procedure aimed at treating this disease by implanting a bioprosthetic valve within the diseased native valve via a catheter delivery system (*4*).

Like any medical procedure, TAVR can be subject to postoperative complications, including paravalvular leak (PVL) and conduction disturbances. PVL is caused by an insufficient seal and presence of gaps between the bioprosthetic valve frame and the native aortic annulus, leading to regurgitation of blood flow from the aorta to the left ventricle (*6*). Post-TAVR conduction disturbances can be triggered by physical interactions between the bioprosthetic valve frame and the anatomy in the critical region proximal to the atrioventricular conduction pathway of the heart and the pressure imposed on this region by the bioprosthetic valve frame (Fig. 1A) (*7*, *8*). This critical region is identified as the lower limit of the membranous septum where the left bundle branch emerges from the His bundle (Fig. 1A) (*7*–*11*). Applied pressure on this region can result in left bundle branch block or atrioventricular block and, ultimately, the need for permanent pacemaker implantation (*7*–*11*).

Several factors related to a given patient's anatomy, the procedure, and the bioprosthetic valve can contribute to post-TAVR complications, including the membranous septum length, septal wall thickness, calcification distribution patterns, patient-prosthesis size mismatch, implantation depth, mispositioning, and type of the bioprosthetic valve (*7*, *11*–*18*). Therefore, the proper selection and optimization of the interplay among these factors based on each patient's unique anatomical features are vital in TAVR planning to mitigate the risk of postoperative complications and mortality.

Compared to surgical aortic valve replacement, where surgeons have direct access to the aortic root anatomy and resect the native calcified valve, the minimally invasive nature of the TAVR procedure can potentially raise the level of difficulty, in terms of full visualization of the anatomical features and their interactions with the bioprosthetic valve (*17*). Currently, most of the decision-making process in TAVR, which includes choosing the correct bioprosthetic valve size, implantation depth, and positioning of the bioprosthetic valve, occurs on the basis of measurements derived from pre- and intraprocedural imaging. This increases the dependency on the clinician's skills and experience and the likelihood of postoperative complications (*17*).

Alternatively, using three-dimensional (3D) printed, patient-specific organ models could enhance the 3D visualization and augment the understanding of the physical interactions between the bioprosthetic valve and the patient's native anatomy, thereby improving preprocedural planning (*19*–*21*). Previous efforts on using 3D printed aortic root models for TAVR were mainly focused on exploring the applications of these models for preprocedural prosthetic fit testing, evaluation of patients' anatomical features, and/or hemodynamic studies for prediction of PVL (*20*–*25*). Most of

[1]Department of Mechanical Engineering, University of Minnesota, Minneapolis, MN 55455, USA. [2]Department of Biomedical Engineering, University of Minnesota, Minneapolis, MN 55455, USA. [3]Department of Surgery, University of Minnesota, Minneapolis, MN 55455, USA. [4]Medtronic, Mounds View, MN 55112, USA. [5]Institute for Engineering in Medicine, University of Minnesota, Minneapolis, MN 55455, USA.
*These authors contributed equally to this work.
†Corresponding author. Email: mcalpine@umn.edu

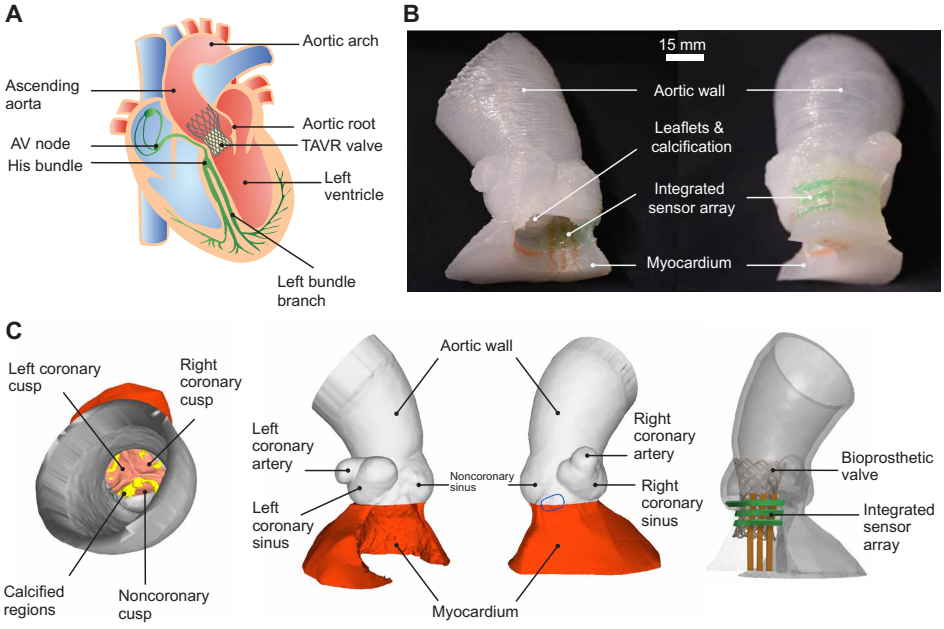

Fig. 1. Overview of the patient-specific, 3D printed aortic root model concept and components. (**A**) Schematic of the heart with implanted TAVR prosthesis in the aortic root region. AV, atrioventricular. (**B**) 3D printed aortic root model with internally integrated sensor array. Photo credit: Ghazaleh Haghiashtiani and Kaiyan Qiu, University of Minnesota. (**C**) Different components of the aortic root model. The calcified regions are shown in yellow. The approximate region of the membranous septum is indicated with the blue marking.

these previously reported models were 3D printed using a single rubber-like commercial photopolymer for mimicking the tissue components of the aortic root structure, including the left ventricle outflow tract, the leaflets, and the aorta, and a rigid material for replicating the calcified lesions on the leaflets (*20*–*25*).

Here, we demonstrated the 3D printing of multimaterial, patient-specific models of the aortic root with the integration of an internal sensor array and evaluated the efficacy of the models by comparison with corresponding patient's data. Specifically, the models comprised three different materials with properties commensurate to (i) the aorta, (ii) the myocardium and leaflets, and (iii) the calcified regions. It should be noted that given the thinness of human aortic leaflets [ca. 600 μm; (*26*)], the impact of the leaflets' mechanical properties is assumed to be negligible, relative to the calcification and other surrounding tissue; hence, the leaflets were approximated with similar properties to the myocardium. Moreover, the internal integration of the sensor array (Fig. 1B), which was simultaneously printed within the anatomical structure, can facilitate the visualization of the contact pressures and critical locations in the region of interest for different cases of bioprosthetic valve sizing and implantation height.

These models can be applied for TAVR preprocedural planning and potentially inform prosthetic device sizing and procedure parameters, patient- and disease-specific hemodynamic assessment, and possible PVL pathways. In addition, these models may provide clinicians with a comprehensive benchtop tool for understanding the deployment of the valve and mitigating some of the risks of post-TAVR conduction disturbances.

RESULTS

Material selection and model fabrication

To initiate the 3D printing process, we obtained computed tomography (CT) scans of the patients' cardiac anatomies, segmented the regions of interest from the images, and then generated the stereolithography (STL) files for the 3D printing process (fig. S1). The models consisted of the aortic wall, a portion of the myocardium, leaflets, and calcifications (Fig. 1C), which were 3D printed simultaneously on the same platform using customized materials that mimic the mechanical properties of their biological counterparts (movie S1).

Formulating customized polymeric 3D printing materials is a fundamental step in the fabrication of these aortic root models. We have previously demonstrated the 3D printing of customized silicone-based polymeric inks for accurately mimicking the physical properties of prostate tissue (*19*, *27*). Our material system mainly consisted of silicone sealant and silicone grease. The silicone sealant was used as the active agent for vulcanization to stabilize the structure, while silicone grease was added as the bulking agent for providing softness and flexibility. The silicone sealant used in this work is an acetoxy silicone, which cures on the basis of a condensation reaction. After printing the material and full exposure to ambient moisture, the acetoxy groups in the material are hydrolyzed to facilitate the condensation process. Coloring agent was also optionally added into the material system to indicate different model sections and/or for the target valve implantation depth mark. This material system has several advantages, including adjustable properties, facile preparation, good printability, and room temperature vulcanization (*19*, *27*).

By adjusting the weight ratio of bulking agent (B) to active agent (A) for different ink formulations, the properties of the customized polymeric inks can be altered to replicate the various soft tissue mechanical properties. As shown in Fig. 2A, by increasing the weight ratio of the bulking to active agent from 0 to 2.05, the corresponding values of Young's moduli decreased from 677.6 ± 28.8 kPa to 37.5 ± 1.9 kPa, i.e., by more than one order of magnitude. The Young's moduli of the inks fall in the broad range of values common for myocardium and aortic tissues (table S1). Hence, this trend

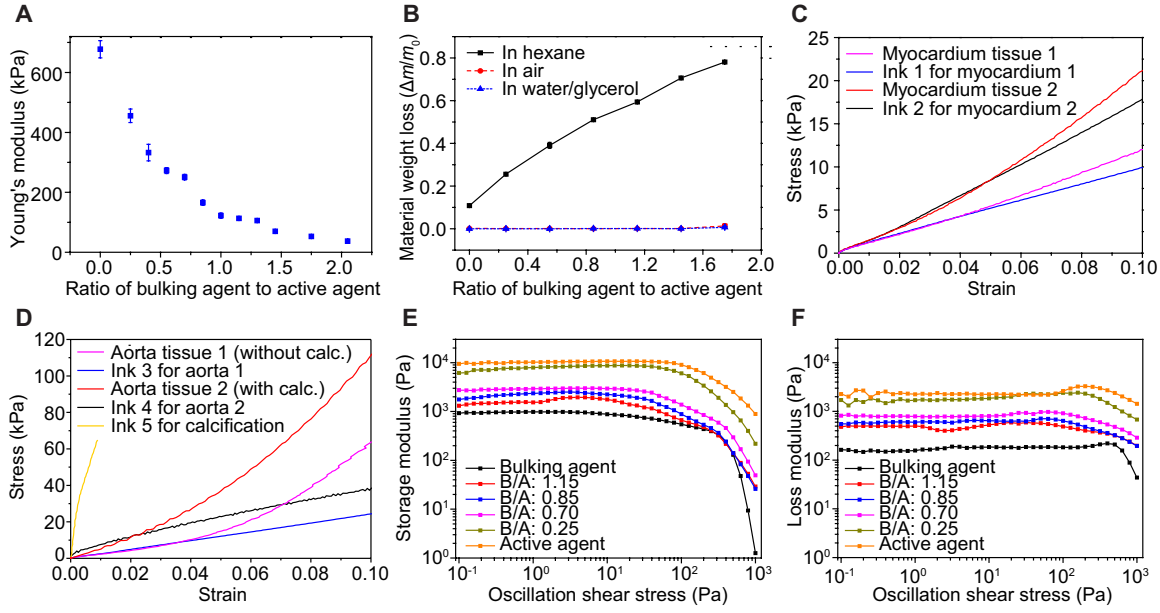

Fig. 2. Characterization of material properties. (**A**) Young's modulus (<3% strain) of the custom-formulated polymeric material versus different weight ratios of the components ($n = 3$). (**B**) Ratio of material weight loss after 96 hours for different compositions of the customized polymeric material upon immersion in hexane, air, and a water/glycerol solution ($n = 3$). (**C**) Stress-strain plots of myocardium tissue specimens and corresponding polymeric materials. (**D**) Stress-strain plots of aortic tissue specimens and corresponding polymeric materials, as well as the calcification materials. (**E**) Oscillatory rheology data of the storage modulus of different custom-formulated polymeric inks and comparison to active and bulking agents. (**F**) Oscillatory rheology data of the loss modulus of different custom-formulated polymeric inks and comparison to active and bulking agents. B/A represents the weight ratio of bulking agent to active agent.

can be used to tailor the mechanical properties of the inks to simulate patient-specific aortic and myocardium tissues. The tunability of the mechanical properties of this material system via adjustment of the component ratios was correlated to the cross-linking density. To verify this, we performed a sol-gel fraction analysis test by immersing samples of the polymeric materials with different component ratios in the organic solvent hexane. It was observed that as the weight ratio of bulking agent to active agent increased from 0 to 1.75, the corresponding normalized weight loss of the materials ($\Delta m/m_0$, where m_0 represents the initial dry weight of the materials and Δm corresponds to the change in weight) following 96 hours of immersion in the solvent increased from 10.9 to 78.1% (Fig. 2B and fig. S2A). This trend correlated with the weight ratio of bulking agent (silicone grease) in the formulation (which is not actively involved in the ink cross-linking), as well as the noncross-linked components in the active agent (silicone sealant), thereby confirming that increasing the weight ratio of bulking agent in the composition results in softer materials.

Given that the 3D printed models in this study will primarily be used in air and a blood-mimicking solution comprising water and glycerol, we investigated the stability of the materials with different formulations in these two environments. The results showed that different formulations of the polymeric material (B/A ranging from 0 to 1.75) were stable without any notable weight loss following 96 hours of exposure to the ambient air environment, as well as immersion in the water/glycerol solution (Fig. 2B). This confirmed that the 3D printed models using these custom-formulated inks can maintain stable properties for applications conducted in these test environments.

After investigating the mechanical properties of the 3D printing materials with different compositions, we compared their mechanical behaviors with tissue specimens of human hearts to select proper formulations for mimicking the properties of the myocardium and aortic wall. In general, the mechanical properties of the soft tissues can vary depending on factors including the subjects (humans or animals) and their ages, disease states, location/orientation of tissue excisions, and the test parameters (*28*). For the purposes of this study, we compared the stress-strain curves of representative tissue samples from human aortic wall and myocardium to the printed samples of the inks with different formulations. It was observed that at small strains (0 to 0.05), the customized polymeric inks 1 and 2, corresponding to formulations with weight ratios of bulking agent to active agent of 1.15 and 0.85, matched the general trends of stress-strain curves of human myocardium tissue samples 1 and 2, respectively (Fig. 2C). The Young's moduli (<3% strain) for representative samples of ink 1 (109.3 kPa) and ink 2 (156.2 kPa) were analogous to myocardium tissue sample 1 (105.3 kPa) and sample 2 (146.4 kPa). At the same strain range (0 to 0.05), the customized polymeric inks 3 and 4 with bulking-to-active weight ratios of 0.70 and 0.25 matched the trends of stress-strain curves of human aortic tissue sample 1 (from a subject without calcification) and sample 2 (from a subject with calcification), respectively (Fig. 2D). The Young's moduli (<3% strain) for representative samples of ink 3 (240.3 kPa) and ink 4 (493.5 kPa) were analogous to the aortic tissue sample 1 (216.1 kPa) and sample 2 (586.5 kPa). At higher strain ranges, a divergence was observed in the stress-strain curves of polymeric materials compared with tissue specimens, which was more notable for the aortic tissue (Fig. 2, C and D). This divergence is largely due to the strain-stiffening behavior of soft tissue structures as a result of collagen fiber alignments and straightening along the load direction at higher strains (*29*). Nevertheless, the modulus values of our developed materials and tested myocardium and aortic tissue

sample were in accord with the range of moduli reported for myocardium (12 to 273 kPa) (*30*, *31*) and aorta (334 to 1817 kPa; table S1) (*32*, *33*).

In addition, we used a spackling material (ink 5) for printing the calcified lesions on the leaflets because of its good printability and comparable mechanical properties to aortic valve calcification. This material contained calcium carbonate as verified by the prominent absorption peaks of CO_3^{2-} at ~712, ~875, and ~1425 cm^{-1} observed in Fourier transform infrared spectroscopy (FTIR) spectra (fig. S2B) (*34*). The Young's modulus of the calcification material was estimated to be 11.8 ± 3.1 MPa (Fig. 2D), which was within a factor of 2 of the reported values of 22.6 ± 9.2 MPa for calcified aortic valve regions (*35*).

Last, the rheological properties of the inks with different formulations were characterized. The customized ink formulations exhibited a shear thinning behavior that facilitates the flow of the inks through the extrusion nozzles during the 3D printing process (*36*). Specifically, as the shear rate increased from 10^{-1} to 10^{3} s^{-1}, the apparent viscosity of the inks decreased from about 10^{3} to 1 Pa·s (fig. S2C). In addition, the inks exhibited yield stress behavior (Fig. 2, E and F), which was advantageous for the 3D printing process (*36*). Applying pressures beyond the yield point to the ink during printing allowed for extrusion of the ink through the nozzle via a decrease in the storage modulus (G') to a value lower than loss modulus (G'') (viscous liquid-like behavior). Once the ink was deposited and the shear stress on the material was relieved, the storage modulus increased to its plateau value in the linear viscoelastic region (in the range of 10^{3} to 10^{4} Pa for the formulations used in this study), which facilitated the shape retention of the deposited ink ($G' > G''$, solid-like behavior).

Model fidelity analyses compared to patient data

After 3D printing the patient-specific aortic root model, a quantitative surface comparison was conducted to evaluate the anatomic fidelity between the model and the corresponding patient's aortic root anatomy via a 3D registration technique (*27*, *37*). The anatomical information of the patient's aortic root was extracted from the preoperative CT scans (fig. S1). The corresponding 3D printed aortic root model was also scanned by CT, and then the CT image stack (Fig. 3A) was used to reconstruct an STL model. A calibrated distance map (Fig. 3B) and a histogram of the calibrated distances (Fig. 3C) were generated from an overlay of the 3D printed model using the corresponding patient's aortic root geometry as the template. The results indicated that most of the calibrated distance points scatter from −3 to 3 mm, with peaks close to 0 mm (Fig. 3, B and C). The fractions of voxels of the 3D printed models within 5, 3, and 1 mm of the patient aortic root geometry were found to be 91.3, 78.9, and 43.6%, respectively (Fig. 3, B and C).

In addition, the TAVR bioprosthetic valve was implanted into the 3D printed aortic root model, which was mounted in a constraining fixture to simulate the surrounding anatomy (fig. S3A). The outcome was compared to the patient's postoperative data via CT imaging (Fig. 3D). It was observed that the locations of displaced leaflet calcifications on the aortic wall in the model after valve implantation were analogous to those of the patient's postoperative scans (Fig. 3D). In addition, the diameter of the bioprosthetic valve was subject to change after implantation in the aortic root, which can be used as another metric for evaluating the fidelity of the 3D printed aortic root models in comparison with the patient's anatomy. To this end, we evaluated the changes in diameter of the implanted bioprosthetic valve at nine different frame node levels (fig. S3B).

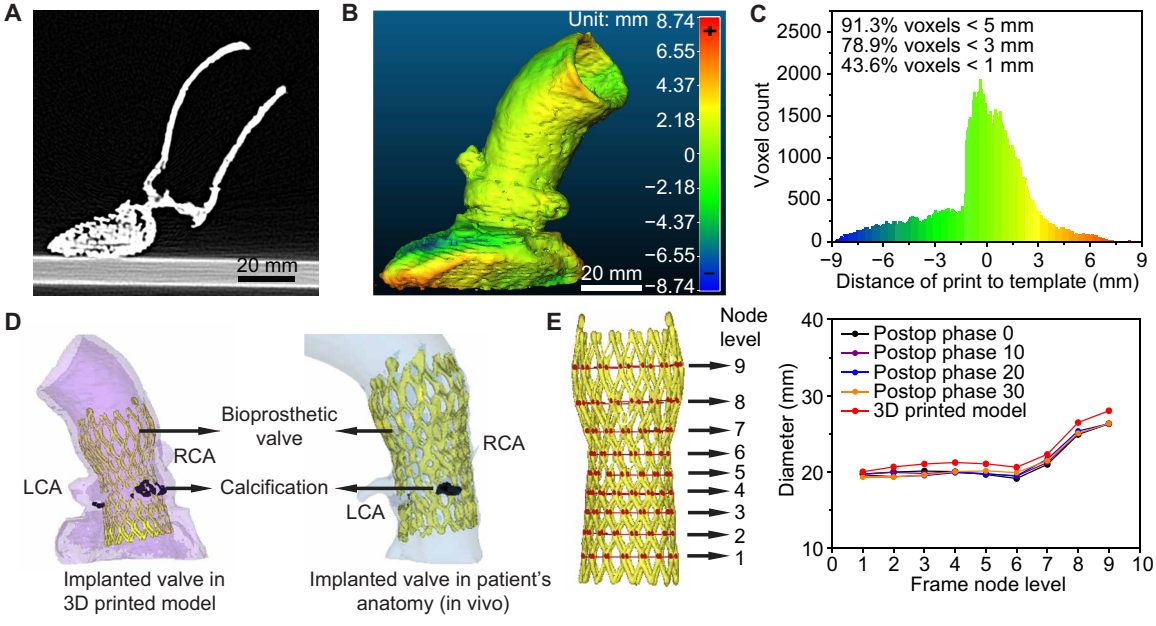

Fig. 3. Anatomical fidelity analyses of the 3D printed aortic root models and comparison to patient postoperative data. (**A**) CT scan of the 3D printed aortic root model. (**B**) Calibrated distance map comparing the anatomical fidelity of the 3D printed aortic root model with the patient's anatomy. (**C**) Histogram of the calibrated distances between the surface points of the 3D printed aortic root model and the patient's anatomy. (**D**) Comparison of the implanted TAVR prosthesis in the 3D printed model with the patient's postoperative data. RCA, right coronary artery; LCA, left coronary artery. (**E**) Comparison of changes in frame diameters of the implanted valve in the 3D printed model with the patient's postoperative data at nine different node levels.

The results showed that the diameter values of the implanted valve in the 3D printed model were close to the patient's corresponding postoperative data at different systolic phases of the cardiac cycle (Fig. 3E). A maximum difference of 6.5% (node level 3) and a minimum difference of 2.2% (node level 1) between the diameter of the implanted valve in the 3D printed model and the average of diameters over the four systolic phases (phases 0, 10, 20, and 30) of the patient's postoperative data were obtained, hence verifying the fidelity of this 3D printed model compared to the patient's anatomy and corresponding physical behavior.

In vitro hemodynamic studies

To capture the hemodynamic performances of the 3D printed aortic root models, we evaluated their in vitro responses in pulsatile flow cycles. For this purpose, we fabricated two sets of models corresponding to normal and stenotic cases: Set 1 are models that were printed using ink 1 for the myocardium and leaflets (lower modulus) and ink 3 for the aortic wall (corresponding to aortic tissue sample 1 from a subject without calcification) and had no calcified regions on the leaflets to represent cases without AS (Fig. 4A); and Set 2 are models that were printed using ink 2 for the myocardium and leaflets [higher modulus; (*38*)] and ink 4 for the aortic wall (corresponding to aortic tissue sample 2 from a subject with calcification) and had calcified regions on the leaflets printed using ink 5 to represent cases with AS (Fig. 4B). The 3D printed models were placed in a custom setup (fig. S4) connected to a pulsatile blood pump. To mimic the dynamic viscosity (3.45 mPa/s) and density (1060 kg/m^3) of blood (*39*), we used a solution composed of water and glycerol with a weight ratio of 6:4 as the working fluid in these tests (dynamic viscosity of ca. 3.3 mPa/s and density of ca. 1098 kg/m^3). The pulsatile

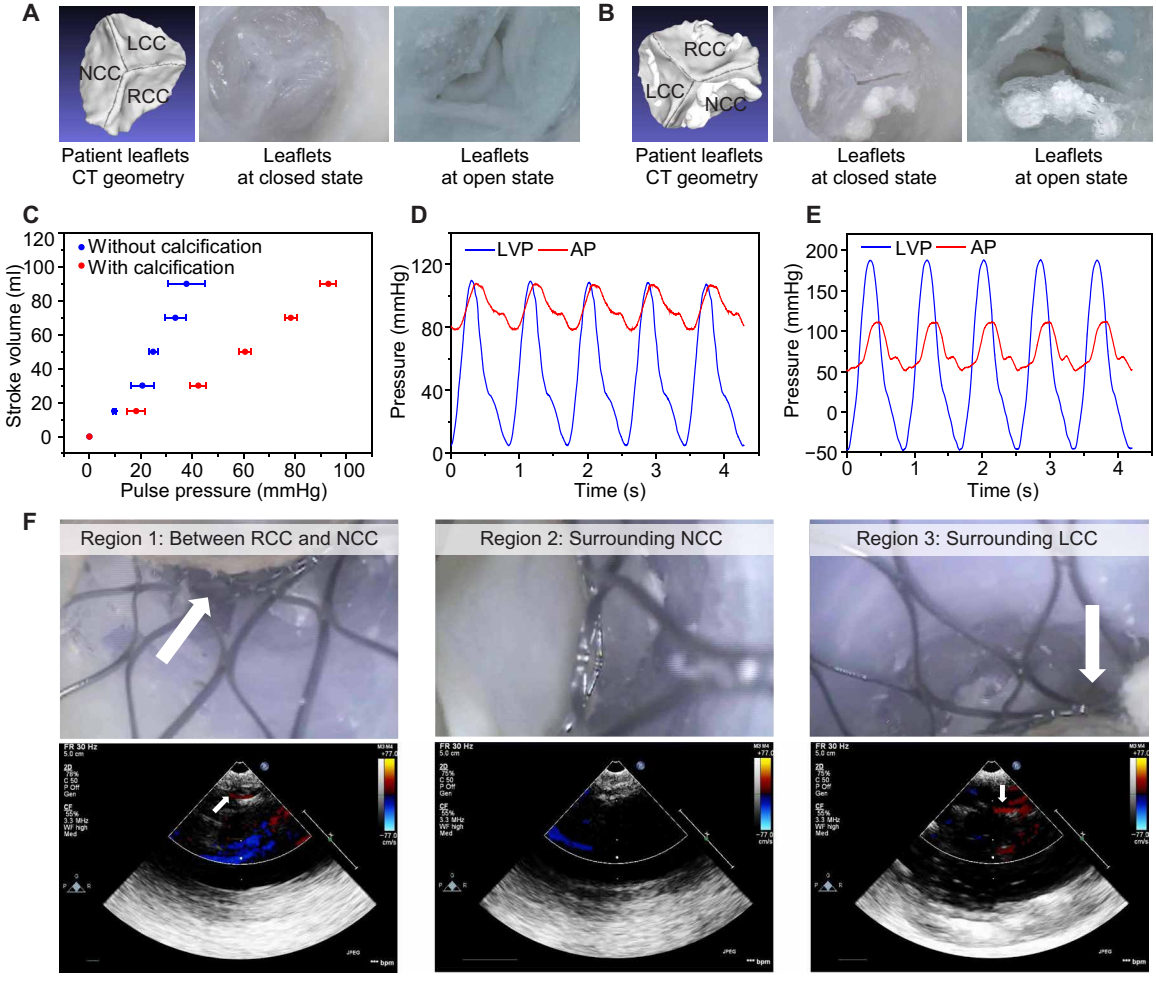

Fig. 4. In vitro hemodynamic studies with the 3D printed aortic root models. (**A**) Leaflets of the 3D printed models without calcification (Set 1) at open and closed states used for in vitro hemodynamic evaluation. Photo credit: Ghazaleh Haghiashtiani, Kaiyan Qiu, and Jorge D. Zhingre Sanchez, University of Minnesota. (**B**) Leaflets of the 3D printed models with calcification (Set 2) at open and closed states used for in vitro hemodynamic evaluations. Photo credit: Ghazaleh Haghiashtiani, Kaiyan Qiu, and Jorge D. Zhingre Sanchez, University of Minnesota. (**C**) Comparison of compliance of models in Set 1 (without calcification; $n = 3$) and Set 2 (with calcification; $n = 3$). (**D**) Changes in left ventricle pressures (LVPs) and aortic pressures (APs) for model without calcification in consecutive pulsatile flow cycles. (**E**) Changes in left ventricle pressures and aortic pressures for model with calcification in consecutive pulsatile flow cycles. (**F**) Detection of potential PVL sites (indicated by the white arrows) in the 3D printed aortic root model with implanted valve and corresponding color Doppler echocardiographs (left, middle, and right panels correspond to regions 1, 2, and 3, respectively). RCC, LCC, and NCC denote right coronary cusp, left coronary cusp, and noncoronary cusp, respectively. Photo credit: Ghazaleh Haghiashtiani, Kaiyan Qiu, and Jorge D. Zhingre Sanchez, University of Minnesota.

pump parameters were adjusted to replicate the physiological conditions in each case. During each flow cycle, upon the increase of the ventricular pressure to a value greater than the aortic pressure, the aortic valves opened and allowed for ejection of the fluid flow from the ventricle into the aorta (systole phase). Once the ventricular pressure reached a value below the aortic pressure, the aortic valve closed (diastole phase; movie S2).

During physiological cardiac cycles, the ejection of blood from the left ventricle to the aorta results in an increase in the aortic pressure. The maximum change in aortic pressure is referred to as the pulse pressure (*PP*) and is defined as the difference between the maximum aortic pressure in systole and its minimum value in diastole (*40*). At a constant stroke volume (*SV*), the amount of pulse pressure depends on the aortic compliance (*C*), which is a property of the aorta that allows for its expansion to accommodate the increase in pressure during blood ejection (*41*). The total aortic compliance can be estimated as the ratio of the stroke volume to the pulse pressure ($C \sim SV/PP$) (*42*). In other words, higher arterial compliance results in smaller values of pulse pressure, at a specific stroke volume. Various factors, such as aging, can result in decreased arterial compliances, mainly due to changes in arterial wall matrix compositions. Specifically, aging has been associated with an increase in collagen content and cross-linking, as well as fragmentation of elastin fibers in the aortic wall, which ultimately leads to arteries with higher stiffnesses and lower compliances in the elderly (*2*). Given the predominant age group of individuals suffering from AS, reduced aortic compliance is a prevalent condition in these patients (*43*).

The capability to capture these changes in aortic compliance would be valuable for in vitro characterizations of transvalvular flows in AS cases with different severity conditions for potential implications in validation of computer flow dynamic models with blood and the development of vascular implants (*20*, *44*). For this purpose, we compared the compliance of the two sets of models by varying the stroke volumes from 15 to 90 ml per stroke and measuring the changes in pulse pressures (Fig. 4C). It was observed that the models in Set 2 with calcified leaflets exhibited lower compliance and, as a result, had higher pulse pressure at a given stroke volume compared to the models in Set 1. The estimated overall compliance for models in Set 1 and Set 2 were 2.11 and 0.90 ml/mmHg, respectively, which were close to the values reported for normal cases (1.91 ± 0.76 ml/mmHg) (*42*) and cases with moderate aortic AS and low aortic compliances (0.90 ± 0.17 ml/mmHg) (*40*). The observed lower compliance of the models in Set 2 compared with Set 1 was also consistent with the higher elastic modulus of ink 4 compared with ink 3 as shown in Fig. 2D.

Another hemodynamic marker in patients with AS is elevated transvalvular pressure gradients between the left ventricle and the aorta during systole (*45*). This is typically caused by valvular obstructions and reduced arterial compliance, which ultimately results in increased left ventricular pressure overloads and dysfunction (*43*, *46*). To this end, we examined the pressure changes in flows across the aortic valve, from the left ventricle outflow tract to the aorta of the 3D printed models with and without calcification. These models were able to replicate the expected trends of pressure changes observed in real cases of normal and stenotic valves. Specifically, it was observed that the model without calcifications yielded almost similar values for the ventricular and aortic pressures during the systole phase of the cardiac cycle, due to the free flow of the fluid from the left ventricle to the aorta, yielding an average of 1.23 mmHg peak-to-peak pressure gradient (Fig. 4D). On the other hand, for the model with calcifications, a higher gradient with an average value of 76.32 mmHg peak-to-peak pressure gradient was observed from the left ventricle to the aorta (Fig. 4E), which falls in the range of reported values for peak-to-peak pressure gradients in patients diagnosed with AS (*47*, *48*).

Last, we implanted a bioprosthetic transcatheter valve in the aortic root model with calcified leaflets (movie S3) and assessed the appositions of the valve frame with the aortic annulus to identify the potential PVL sites. For this purpose, we selected three regions along the annulus as follows: Region 1 surrounds the commissure between the right coronary cusp and noncoronary cusp; Region 2 surrounds the noncoronary cusp; and Region 3 surrounds the left coronary cusp. We used a videoscope to visualize the appositions of the frame with respect to the aortic wall of the model at these three locations, as well as the color Doppler echocardiography to verify PVL occurrences by evaluating the directions and speeds of the fluid flow in the regions of interest (Fig. 4F). It was observed that an improper seal and existing gaps between the stent frame and the aortic wall of the model at Regions 1 and 3 resulted in some degree of PVL at these locations, which was verified by the presence of eccentric jets and their velocities in the corresponding echocardiograms (*49*). On the other hand, the echocardiogram for Region 2 did not indicate the occurrence of PVL, which was in accordance with the fact that no gaps were visually detected at this location.

Visualization of applied pressures via internally integrated sensor arrays

To quantify the applied pressures on the critical region of the aortic root after bioprosthetic valve implantation, we designed a capacitive pressure sensor array that was internally embedded within the critical landmark of the aortic root models and was in direct contact with the implanted valve. We chose a 3 × 3 array to cover the area surrounding this critical region of interest as a starting point for a proof-of-concept demonstration of tailored, internal integration of these electronics into patient-specific organ models and their simultaneous fabrication. For this purpose, the design of the array was motivated by optimizing the contributions from the patient's anatomical geometry in that region, as well as optimizing printing parameters. Each sensing element in the designed array consisted of two layers of polyacrylamide-based ionic hydrogel as the conductive electrodes that were separated by a dielectric layer composed of the silicone-based material with the same composition as the myocardium sections of the models (Fig. 5A). Applying an external pressure to the sensor results in a deformation of the dielectric elastomer layer and, consequently, changes in device capacitance. To incorporate the sensor array within the model, we integrated two sets of horizontal (green in Fig. 5B) and vertical (orange in Fig. 5B) electrode channels that conformally follow the contour of the anatomy in the model design (fig. S5 and movie S4). After printing and curing of the aortic root models, the channels were then filled by injection of the aqueous solution of the ionically conductive hydrogel, followed by ultraviolet (UV) photopolymerization (Fig. 5B). A sensing element was formed at each crossing junction of these channels.

The internally integrated sensor array was calibrated to map the pressures imposed by the implanted valve on the critical region of the anatomy for different cases of bioprosthetic valve sizes and

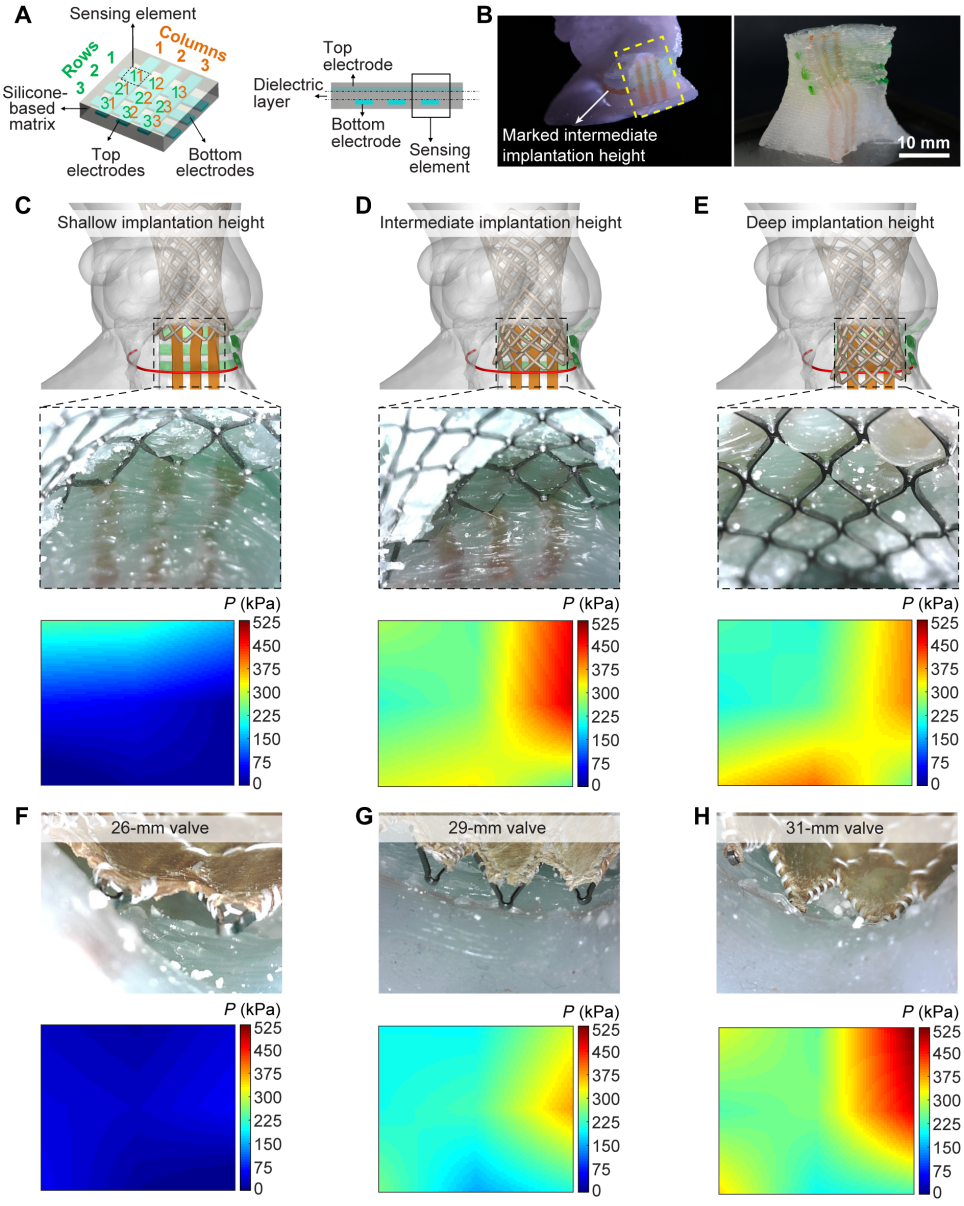

Fig. 5. 3D printed aortic root model with internal sensor arrays and visualization of applied pressures after valve implantation. (**A**) Schematic of the sensor array concept design in planar configuration. (**B**) 3D printed aortic root model with internal sensor array (left) and the corresponding isolated sensor region (right). The vertical (orange) and horizontal (green) electrodes of the integrated sensor arrays on the model correspond to the top and bottom electrodes in the planar design, respectively. (**C**) Implantation of the 29-mm Evolut R TAVR valve frame at a shallow height. (**D**) Implantation of the 29-mm Evolut R TAVR valve frame at an intermediate height. (**E**) Implantation of the 29-mm Evolut R TAVR valve frame at a deep height. The red marked lines in (C) to (E) correspond to the intermediate implantation height. (**F**) Implantation of the 26-mm Evolut R TAVR valve at an intermediate height. (**G**) Implantation of the 29-mm Evolut R TAVR valve at an intermediate height. (**H**) Implantation of the 31-mm CoreValve TAVR valve at an intermediate height. Photo credit for (B) to (H): Ghazaleh Haghiashtiani and Kaiyan Qiu, University of Minnesota.

implantation depths (Fig. 5, C to H). The resulting pressure maps provided quantitative visualizations of the pressure distributions in each of these cases, which, in turn, could be used to optimize the prosthesis implantation heights and alignments within the given anatomy. Specifically, we implanted a 29-mm valve frame at three different implantation heights that yielded estimated maximum pressure values of 234, 486, and 404 kPa, corresponding to implantations at a shallow height (Fig. 5C), intermediate height (Fig. 5D), and deep height (Fig. 5E), respectively. Similarly, we implanted three different TAVR valves with sizes of 26 (Fig. 5F), 29 (Fig. 5G), and 31 mm (Fig. 5H) by keeping the implantation height constant at the intermediate level. The resulting pressure maps showed much lower pressure values for the 26-mm valve case, compared to 29- and 31-mm valve sizes, which correlates with the existence of gaps between the valve frame and the model wall in this case. The estimated maximum pressure values for these cases were 60, 375, and 528 kPa, respectively.

Previous case studies involving computational modeling of the applied pressures on the critical region of the aortic root anatomy after bioprosthetic valve implantation have suggested that conduction

disturbances may occur for maximum contact pressures within 0.43 to 0.7 MPa for the self-expanding CoreValve Evolut R valve (Medtronic) (*8*) and 0.29 to 0.8 MPa for the mechanically expandable LOTUS valve (Boston Scientific), with cutoff values of 0.39 and 0.36 MPa, respectively (*50*). Correlating these values with the pressure readings from the different cases of valve implantations suggests that the patient may experience conduction disturbances with a valve size of 29 mm positioned at the intermediate implantation height. This prediction matched the actual patient outcome, whose anatomy was investigated in this proof-of-concept study.

DISCUSSION

Here, we have demonstrated that the fabrication of multimaterial 3D printed aortic root models with internal sensor arrays are of meaningful research value for different purposes in TAVR testing applications. Specifically, these models can be used to complement the current clinical practices in TAVR preprocedural planning and facilitate the decision-making processes in various AS cases, e.g., those with different levels of disease severities and anatomical intricacies requiring one to carefully select the appropriate type, size, implantation depth, and positioning of the bioprosthetic valve. Thus, these models could aid in alleviating the risks of postoperative complications, as well as in gaining a better understanding of the interplay between the different factors on the outcome based on each patient's unique anatomical features.

These proof-of-concept demonstrations need to be further verified with large-scale, retrospective and prospective clinical studies. Specifically, a large cohort of patients with postoperative heart block should be analyzed, both clinically and via computer simulations, to validate the efficacies of using these 3D printed models for the prediction of potential conduction disturbances and to define contact pressure threshold values for these conduction disturbances with different types of bioprosthetic valves.

Moreover, the mechanical characterization of the tissue and polymeric materials showed a discrepancy between the elastic moduli of the two at higher strain values. Despite this discrepancy, it was observed that the values obtained for aortic compliance of the 3D printed models in the hemodynamic tests fall in the range of reported values for normal and stenotic cases, confirming the validity of these models for in vitro flow studies undergoing higher mechanical strains. Nevertheless, future efforts should be focused on developing 3D printing materials and strategies to better mimic both bulk and surface properties of biological tissues, including heterogeneity, anisotropy, strain-stiffening properties at higher strains (*51*), porosity, wettability, and bioadhesion. Improving the resolutions and sensitivities of the integrated sensor arrays could also pinpoint the localization of regions with critical contact pressures and provide a more accurate representation of pressure distribution, thus improving the efficacies of these models in alleviating potential risks of post-TAVR conduction disturbances.

The concepts outlined in this work aimed to demonstrate the application of 3D printed aortic root models with internal sensors as preplanning platforms for minimally invasive procedures such as TAVR. More broadly, these patient-specific models can be designed with targeted functionalities for a variety of minimally invasive procedures, including, but not limited to, endovascular coiling, sialoendoscopy, coronary angioplasty, and/or stenting. These models could be implemented as surgical adjuncts to address the limited accesses inherent to these types of procedures, i.e., by providing realistic, 3D visualizations of the organs of interest and targeted quantitative feedback for the specified surgical interventions. Hence, the models could ultimately enhance preoperational planning and alleviate some of the risk of intra- and postoperative complications of associated therapies. In addition, these sensing models could serve as a benchtop platform for the development of next-generation prostheses and medical devices. The outcomes of this work could contribute to the incorporation of advanced dynamic functionalities into the organ models, setting the stage for bionic organs, or for "smarter" surgeries by using the models to train robot-assisted, minimally invasive procedures, hence defining a compelling paradigm for the future of personalized medicine.

MATERIALS AND METHODS

3D printing material formulation and preparation

The material system mainly consisted of silicone sealant (acetoxy-based room temperature vulcanizing sealant, LOCTITE SI 595 CL) and silicone grease (LP20, Trident). For ink preparation, the active agent and bulking agent were mixed at specified weight ratios via a planetary centrifugal mixer (ARE-310, THINKY) at 2000 rpm for 6 min to form the customized polymeric inks with different properties. The prepared weight ratios of bulking agent to active agent were 0, 0.25, 0.4, 0.55, 0.70, 0.85, 1.00, 1.15, 1.3, 1.45, 1.75, and 2.05 to achieve different values of Young's modulus and other mechanical properties. Coloring agent (Procinyl Red GS, ICI America Inc.) was optionally added into the material system for the purpose of indicating different model sections or the bioprosthetic valve implantation depth mark. For adding the coloring agent to the material, the customized polymeric ink (10 g) was mixed with 1% (w/v) coloring agent in dichloromethane solution (0.5 ml) at a 20:1 (w/v) ratio via the mixer at 2000 rpm for 6 min. For printing the calcified regions, ALEX PLUS Spackling material (DAP Products Inc.) was used. In addition, during the printing process, a sacrificial ink was used to construct the supporting structures, which comprised the surfactant Pluronic 127 (Sigma-Aldrich) dissolved at a ratio of 40:100 (w/v) in glycerol/deionized water solution (1:9 v/v). After printing and curing of the model, the supporting structure was removed by flushing with cold water.

Sol-gel and stability tests of the customized polymeric materials in glycerol-water, hexane, and air

For analyzing the sol-gel fractions of the customized polymeric materials, rectangular samples were 3D printed with dimensions of 15 mm × 15 mm × 1.2 mm (length × width × height) using different ink formulations (weight ratios of bulking agent to active agent of 0, 0.25, 0.55, 0.85, 1.15, 1.45, and 1.75). First, the samples were weighed to obtain their initial dry weight (m_0) and then were immersed in glycerol-water solution with a volume ratio of 0.65:1.23 (corresponding to the test fluid used in the hemodynamic studies) or hexane solvent in glass vials. The glass vials containing the samples immersed in the test solvent were placed on an orbital shaker (VWR, Model 3500) and maintained at room temperature and ~250 rpm. At time intervals of 24, 48, 72, and 96 hours after immersion, the solid contents of the samples were extracted from the test solution using filter paper (P5 Grade, 09-801B, Thermo Fisher Scientific) to obtain potential residues. For samples immersed in water/glycerol, an additional rinsing step with deionized water was performed after

removal from the solution. Next, these obtained samples were dried, and their dry weights were measured. The measured weights were regarded as the weight of the cross-linked portion of the materials at each time interval (m_i). The weight losses ($\Delta m = m_0 - m_i$) and the ratios of weight loss to initial weight of the samples ($\Delta m/m_0$) were then determined at each time interval as an indicator of the stabilities of the materials in each test solution. Similar measurements were performed by obtaining the weight changes of the samples in ambient air over the course of 96 hours to determine the stabilities of the polymeric materials in air.

Preparation and characterizations of the tissue samples

Human tissue specimens were obtained from myocardium and aortic wall regions. The tissue samples for compression tests were cut using a laser cutter (Helix 24; Epilog Laser) into cylindrical samples. Specifically, the aortic and myocardium tissue specimens were prepared with dimensions of ca. 7.1 to 7.2 mm × 1.5 to 2.4 mm (diameter × height) and ca. 6.6 to 6.7 mm × 2.2 to 3.5 mm (diameter × height), respectively. The cylindrical samples were mounted on a mechanical analyzer (RSA-G2, TA Instruments) for compression tests using an 8-mm parallel plate geometry and were compressed at a strain rate of 0.0355 s^{-1}. It should be noted that a set of human tissue specimens from a calcified aorta were received as rectangular samples and tested in tension to obtain the modulus range for this specific case (aorta tissue 2 and its corresponding ink 4).

Mechanical characterization of the customized polymeric materials

For compression tests, the polymeric materials with different formulations were printed into cylindrical samples with dimensions of ca. 8 mm × 5 mm (diameter × height). For tensile tests, the polymeric ink with specified formulation was printed into rectangular samples with dimensions of ca. 35 mm × 5 mm × 1 mm (length × width × thickness, as printed). Both compression and tensile tests were carried out using a mechanical analyzer (RSA-G2, TA Instruments). An 8-mm parallel plate geometry was used in compression tests. The test procedure and settings were the same as the tissue characterization for comparison purposes.

Rheological characterization of the customized polymeric inks

Rheological characterization of the customized polymeric inks and their main constituents were performed on a magnetic-bearing rheometer (AR-G2, TA Instruments) with a steel plate (25-mm diameter) Smart Swap geometry at 25°C. Viscometry experiments were conducted via a logarithmic sweep of shear rate at 0.1 to 1000 s^{-1} range with a 500-μm gap between the Smart Swap geometry and the lower geometry. Oscillatory rheometric experiments were conducted via a logarithmic sweep of oscillation shear stress at 0.1 to 1000 Pa range and a frequency of 1 Hz with a 500-μm gap between the Smart Swap geometry and the lower geometry.

Fourier transform infrared spectroscopy

Chemical analyses of the spackling material were carried out using an FTIR spectrophotometer (Thermo Fisher Scientific Nicolet iS50) in attenuated total reflection mode. Spectra, averaged over 32 scans, were taken in the range of 4000 to 400 cm^{-1} wave number, at a resolution of 4 cm^{-1}.

Processing of STL models

Two patient-specific aortic root STL models, derived from CT images, were received from Medtronic plc. Each STL model consisted of the aortic wall, myocardium, leaflets, and calcifications. For the purpose of this study, the first patient anatomy was used for fidelity analysis experiments (Fig. 3), and the second patient anatomy was used for hemodynamic studies (Fig. 4; for case studies with and without calcification, the calcified regions were included/excluded, correspondingly) and sensor integration (Fig. 5). To 3D print a part, the STL models were sliced into horizontal layers (fig. S1) and converted into G-code, the computer language that dictated the printing pathways as the inputs for the 3D printing process. MeshLab, an open source mesh processing system, was used to divide each STL model into separate components (myocardium, aortic wall, leaflets, and calcifications) to facilitate the assignment of different inks and their corresponding settings for the printing process. Slic3r, an open source slicing software, was used for slicing these models into layers and G-code generation. We imported the full aortic root models into Slic3r, as well as the separate component STL files as modifiers. These modifiers allowed for assignment of different inks, print speeds, perimeters, and other printing parameters for specific regions of a given model. When each model was fully configured for printing, Slic3r was used to generate the G-code. Last, a custom MATLAB script was used to convert the G-code generated from Slic3r into a form compatible with our custom-built 3D printing system for multinozzle printing.

3D printing of aortic root models

A custom-built 3D printing system (AGS1000, Aerotech) with two independent z-axis heads was used for 3D printing of aortic root models. Four inks with different properties, including the ink for aortic wall, the ink for myocardium and leaflets, the ink for calcified region, and the ink for supporting material, were used in the process and were deposited from four dispensing apparatuses controlled by four high-precision dispensers (Ultimus V, Nordson EFD). For fabricating the models used for fidelity analyses and hemodynamic studies, the myocardium section and its corresponding support structure were printed using nozzles with an inner diameter of 1.36 mm (15GA GP .054X.25, Nordson EFD) and layer height of 1.2 mm, and the leaflets, aortic wall, calcification, and their corresponding supporting structure were printed using nozzles with an inner diameter of 0.84 mm (18 GA GP .033X.25, Nordson EFD) and layer height of 0.7 mm. For these cases, the printing speeds for perimeter and infill of the models were set to 20 and 10 mm/s, respectively. For fabricating the models with integrated sensors, finer nozzles (inner diameter of 0.51 mm, 21 GA GP .020X.25, Nordson EFD) and layer height (0.4 mm) were used for the lower section of the model (myocardium and aortic root including the sinuses, leaflets, and calcification) to 3D print the sensor array with a higher resolution. The top parts of these models (ascending aorta) were printed using nozzles with an inner diameter of 1.36 mm and a layer height of 1.2 mm. The printing speeds for perimeter and infill of these models were set to 10 and 8 mm/s, respectively. After printing, the models were left in ambient air for 5 to 7 days to ensure complete curing. Once the models were fully cured, the supporting structure was removed via flushing with cold water. Two cases of patient-specific aortic root models were printed, one for fidelity analysis and one for hemodynamic studies and sensor integration.

Model fidelity analyses

To assess the fidelities of the 3D printed structures to the patient anatomies, a CT scan was performed on the 3D printed aortic root model. The obtained CT image stack was then segmented and converted to a 3D aortic root model with an STL format using Mimics Medical 21.0 (Materialise NV) software package. 3D registration of the STL files between the 3D printed aortic root model and the patient aortic root geometry was achieved using CloudCompare 2.10.2 (www.cloudcompare.org) open source software. CloudCompare was also used to overlay the two 3D models and obtain a distance map along with a histogram of the offset between the patient anatomy as the template and the 3D printed construct for 3×10^5 voxels in 40 iterations. It should be noted that the 3D printed model geometry can experience deformation under its own weight due to gravity, while for the patient case, the aortic root is constrained by the surrounding anatomy. Hence, to minimize the impact of deformations due to gravity, the two 3D models were overlaid by matching the ascending aorta as the reference region.

After registration, the two models were compared using the cloud to mesh tool in CloudCompare. The process generated a distance heatmap and a histogram of the distance differences between the points of the 3D printed model and the patient's native aortic root anatomy. The distance scale in CloudCompare was then calibrated to millimeters. From the histogram of the distances, the print fidelity was determined by the percentile of points that fell between a given error margin.

Frame analysis study on the 3D printed aortic root model with implanted valve

A 26-mm Evolut PRO (Medtronic) valve frame was implanted into the 3D printed aortic root model using the EnVeo PRO delivery system. The model was also mounted in a fixture for mimicking the confinement and the surrounding structure of the aortic root in the patient anatomy (fig. S3). After performing the CT scans, the aortic root and the valve frame were computationally modeled and reconstructed using the Mimics Medical 21.0 (Materialise NV) software package. A total of nine splines were added at different levels of the reconstructed frame for the purpose of frame deformation analysis and comparison to the corresponding patient's postoperative frame dimensions.

In vitro hemodynamic testing and parameter calculation

The hemodynamic studies were performed using a test setup (fig. S4) consisting of a pulsatile piston blood pump for simulating cyclic flow (Model 1423, Harvard Apparatus), an endoscopic videoscope (IPLEX FX Model IV8000 IV6C6-13, Olympus) for direct visualization of leaflet movements, a flow probe sensor for measuring the volumetric flow rates (ME 13 PXN Inline Flowsensor, Transonic), two pressure catheters for monitoring the ventricular and aortic pressures [a balloon pressure catheter (Attain Venogram Balloon Catheter 6215-80 cm, Medtronic) and a syringe-based pressure catheter], a silicone-based fixture (Mold Star 15, Smooth-On) for constraining the models, a fluid reservoir, and an arterial compliance chamber. The height of the arterial compliance chamber in the setup was adjusted to provide the approximate baseline diastolic aortic pressures under different testing conditions. Silicone tubing was used to connect the components to each other and to the 3D printed aortic root models. The working fluid was a solution comprising water and glycerol with a weight ratio of 6:4. The pump settings were adjusted to provide a rate of 70 beats/min and an output phase ratio (% systole/% diastole) of 50/50 for all tests. The values of stroke volume were adjusted for different tests. Specifically, for investigating the compliance of the models (Fig. 4C), the tests were performed at stroke volumes of 15, 30, 50, 70, and 90 ml per stroke. For evaluating the pressure changes in the model without calcification (Fig. 4D), the stroke volume was set to 70 ml per stroke and the baseline diastolic aortic pressure was adjusted to ~80 mmHg. For the model with calcification (Fig. 4E), the stroke volume and the baseline diastolic aortic pressure were adjusted to 50 ml per stroke and ~50 mmHg, respectively (*52*).

The values of pulse pressure in Fig. 4C were calculated by subtracting the average systolic aortic pressure and the average diastolic aortic pressure over 10 consecutive cycles. The data points and the error bars in the plot corresponded to the average and SD of three tested models for each case, respectively. The estimated values of overall compliance corresponded to the slope of the linear fit for each case.

The peak-to-peak pressure gradient values corresponding to Fig. 4 (D and E) were calculated by averaging the difference between the maximum ventricular pressure and the maximum aortic pressure in systole over 10 consecutive cycles. If applicable, the readings for left ventricular pressure were adjusted on the basis of the calibration baseline of the corresponding balloon pressure catheter. The negative values of left ventricular pressure at the beginning of diastole correspond to the instant when the pulsatile pump stops and most of the fluid is pushed out through the leaflets and into the aorta. At this moment, there is less fluid pressure in the left ventricular; thus, the pressure reading in LV is negative.

For PVL study, a 26-mm Medtronic Evolut R (Medtronic) valve was implanted in the model with calcified leaflets. Transthoracic echocardiograms of the 3D printed aortic root model with implanted valve for detection of PVL sites were obtained from a long-axis view via an ultrasound system (Model iE33, Philips) using an X7-2 pediatric probe (Philips).

Preparation of models with internally integrated sensor arrays

The ionic hydrogel precursor used to create the electrodes of the sensor consisted of acrylamide monomer (A8887, Sigma-Aldrich) dissolved in an 8 M lithium chloride solution (L7026, Sigma-Aldrich) with a ratio of 15.64:100 (w/v), as well as *N*,*N*′-methylenebisacrylamide cross-linking agent (M7279, Sigma-Aldrich) and 2-hydroxy-2-methylpropiophenone photoinitiator (405655, Sigma-Aldrich) with ratios of 0.00064:1 and 0.00543:1 with respect to the weight of acrylamide monomer, respectively. For better visualization of the ionic hydrogel in the channels, orange and green dyes were added to the precursor solution [0.5% (v/v)]. Once the 3D printed models were fully cured, the ionic hydrogel precursor was injected into the channels via a 30-gauge needle (305128, BD) and was photopolymerized via exposure to a UV system (OmniCure S1500, Excelitas Technologies). For testing purposes and connection of the sensor array to the measurement system, flexible 28 AWG stranded tinned copper wires (BNTECHGO) were inserted into the filled channels of the models.

Calibration of the sensor array

To translate the capacitance changes of the sensing elements to pressure values, the sensor arrays were quantitatively calibrated. For this purpose, the region of the model limited to the 3×3 sensor array was fabricated separately (Fig. 5B, right). The calibration was performed by individually applying different pressures to each of the nine sensing elements in the array and measuring the changes in

their capacitances. The sensor array was fixed on a silicone-based platform (Mold Star 15, Smooth-On) and was mounted on a digital scale (Elec3) to record the values of applied forces during calibration (fig. S6A). A custom 3D printed bar (tough resin, Formlabs 2) with a rectangular tip with dimensions of 2 mm × 2 mm (approximately corresponding to the area of the sensing elements) was mounted on a vertical axis of a nanopositioning stage (ANT130LZS, Aerotech) to apply a press-release cycle to each sensing element of the device. By varying the vertical positions of the bar during the calibration process, different values of the applied forces were obtained. The applied pressure values were calculated by dividing the recorded forces by the area of the sensing elements before deformation. In addition, the sensor was connected to a characterization system (B1500A, Agilent Technologies) to record the changes in device capacitances at each of the press-release cycles. The recorded measurements were analyzed to obtain plots of $\frac{\Delta C}{C_0}$ versus applied pressure, yielding two regions with different sensitivities corresponding to low-pressure and high-pressure regimes. Hence, to more accurately capture and translate the response of the device, two linear fits corresponding to each regime were used for each of the sensing elements. To translate the capacitance changes to pressures values, the calibration equation corresponding to the appropriate $\frac{\Delta C}{C_0}$ range of each sensing element in the array was used (table S2). The calibration equations are devised with the format of $P = \left(\frac{\Delta C}{C_0} + b\right)/a$, where a represents sensitivity of the sensing elements in each region with units of kPa^{-1}, and b is the intercept of the linear fit.

Testing models with internally integrated sensor arrays

The 3D printed aortic root models were placed in a custom silicone-based fixture (Mold Star 15, Smooth-On) and connected to a characterization system (B1500A, Agilent Technologies) to measure the capacitance values. For each case of valve sizing and implantation height, first, the baseline capacitances of the nine sensing elements in the sensor array were recorded (C_0). Then, the bioprosthetic valve was implanted in the model, followed by measuring the changes in capacitance values. The bioprosthetic valves used in the tests were the Medtronic Evolut R 26 mm, Evolut R 29-mm valve and stent frame, and the CoreValve 31 mm (fig. S7). The normalized capacitance changes $\left(\frac{\Delta C}{C_0}\right)$ of the nine sensing elements for each case of valve sizing and implantation height were then processed using MATLAB to obtain the heatmaps (fig. S8). Given the arrangement of the sensing elements in the array and the relative ratio of the active versus inactive area as depicted in Fig. 5 (i.e., the lateral spacing between adjacent elements being comparable to the dimensions of the active sensing elements), the nine data points were linearly interpolated to obtain the continuous heatmaps for the purpose of providing visual guides and estimation of the pressure distribution. Specifically, using the "interpn" function in MATLAB with linear interpolation method, the intervals were consecutively halved five times in each dimension, resulting in $2^5 - 1 = 31$ interpolated points between the sample data points. To translate the capacitance changes to pressures values, the calibration equations corresponding to each sensing element in the array and the $\frac{\Delta C}{C_0}$ range were used (table S2).

SUPPLEMENTARY MATERIALS

Supplementary material for this article is available at http://advances.sciencemag.org/cgi/content/full/6/35/eabb4641/DC1

View/request a protocol for this paper from *Bio-protocol*.

REFERENCES AND NOTES

1. J. Vespa, D. M. Armstrong, L. Medina, *Demographic turning points for the United States: population projections for 2020 to 2060* (U.S. Department of Commerce, Economics and Statistics Administration, 2018).
2. J. L. Fleg, J. Strait, Age-associated changes in cardiovascular structure and function: A fertile milieu for future disease. *Heart Fail. Rev.* **17**, 545–554 (2012).
3. R. L. Osnabrugge, D. Mylotte, S. J. Head, N. M. Van Mieghem, V. T. Nkomo, C. M. LeReun, A. J. Bogers, N. Piazza, A. P. Kappetein, Aortic stenosis in the elderly: Disease prevalence and number of candidates for transcatheter aortic valve replacement: A meta-analysis and modeling study. *J. Am. Coll. Cardiol.* **62**, 1002–1012 (2013).
4. B. R. Lindman, M.-A. Clavel, P. Mathieu, B. Iung, P. Lancellotti, C. M. Otto, P. Pibarot, Calcific aortic stenosis. *Nat. Rev. Dis. Primers.* **2**, 16006 (2016).
5. N. Bhatia, S. S. Basra, A. H. Skolnick, N. K. Wenger, Aortic valve disease in the older adult. *J. Geriatr. Cardiol.* **13**, 941–944 (2016).
6. M. Eleid, Interventional management of paravalvular leak. *Heart* **104**, 1797–1802 (2018).
7. J. J. Bax, V. Delgado, V. Bapat, H. Baumgartner, J. P. Collet, R. Erbel, C. Hamm, A. P. Kappetein, J. Leipsic, M. B. Leon, P. MacCarthy, N. Piazza, P. Pibarot, W. C. Roberts, J. Rodés-Cabau, P. W. Serruys, M. Thomas, A. Vahanian, J. Webb, J. L. Zamorano, S. Windecker, Open issues in transcatheter aortic valve implantation. Part 2: Procedural issues and outcomes after transcatheter aortic valve implantation. *Eur. Heart J.* **35**, 2639–2654 (2014).
8. G. Rocatello, N. El Faquir, G. De Santis, F. Iannaccone, J. Bosmans, O. De Backer, L. Sondergaard, P. Segers, M. De Beule, P. de Jaegere, Mortier, Patient-specific computer simulation to elucidate the role of contact pressure in the development of new conduction abnormalities after catheter-based implantation of a self-expanding aortic valve. *Circ. Cardiovasc. Interv.* **11**, e005344 (2018).
9. M. Y. Lee, S. C. Yeshwant, S. Chava, D. L. Lustgarten, Mechanisms of heart block after transcatheter aortic valve replacement–cardiac anatomy, clinical predictors and mechanical factors that contribute to permanent pacemaker implantation. *Arrhythm. Electrophysiol. Rev.* **04**, 81–85 (2015).
10. N. Piazza, P. de Jaegere, C. Schultz, A. E. Becker, P. W. Serruys, R. H. Anderson, Anatomy of the aortic valvar complex and its implications for transcatheter implantation of the aortic valve. *Circ. Cardiovasc. Interv.* **1**, 74–81 (2008).
11. B. A. Oestreich, M. Mbai, S. Gurevich, P. S. Nijjar, S. Adabag, S. Bertog, R. Kelly, S. Garcia, Computed tomography (CT) assessment of the membranous septal anatomy prior to transcatheter aortic valve replacement (TAVR) with the balloon-expandable SAPIEN 3 valve. *Cardiovasc. Revasc. Med.* **19**, 626–631 (2018).
12. A. Hamdan, V. Guetta, R. Klempfner, E. Konen, E. Raanani, M. Glikson, O. Goitein, A. Segev, I. Barbash, P. Fefer, D. Spiegelstein, I. Goldenberg, E. Schwammenthal, Inverse relationship between membranous septal length and the risk of atrioventricular block in patients undergoing transcatheter aortic valve implantation. *JACC Cardiovasc. Interv.* **8**, 1218–1228 (2015).
13. R.-J. Nuis, N. M. Van Mieghem, C. J. Schultz, A. Tzikas, R. M. Van der Boon, A.-M. Maugenest, J. Cheng, N. Piazza, R. T. van Domburg, P. W. Serruys, P. P. de Jaegere, Timing and potential mechanisms of new conduction abnormalities during the implantation of the Medtronic CoreValve System in patients with aortic stenosis. *Eur. Heart J.* **32**, 2067–2074 (2011).
14. B. Fujita, M. Kütting, M. Seiffert, S. Scholtz, S. Egron, E. Prashovikj, J. Börgermann, T. Schäfer, W. Scholtz, R. Preuss, J. Gummert, U. Steinseifer, S. M. Ensminger, Calcium distribution patterns of the aortic valve as a risk factor for the need of permanent pacemaker implantation after transcatheter aortic valve implantation. *Eur. J. Echocardiogr.* **17**, 1385–1393 (2016).
15. G. C. Siontis, P. Jüni, T. Pilgrim, S. Stortecky, L. Büllesfeld, B. Meier, P. Wenaweser, S. Windecker, Predictors of permanent pacemaker implantation in patients with severe aortic stenosis undergoing TAVR: A meta-analysis. *J. Am. Coll. Cardiol.* **64**, 129–140 (2014).
16. J. G. Almeida, S. M. Ferreira, P. Fonseca, T. Dias, C. Guerreiro, A. R. Barbosa, P. Teixeira, M. Carvalho, W. Ferreira, N. D. Ferreira, M. Oliveira, H. Gonçalves, P. Braga, J. Ribeiro, J. Primo, V. G. Ribeiro, Association between implantation depth assessed by computed tomography and new-onset conduction disturbances after transcatheter aortic valve implantation. *J. Cardiovasc. Comput. Tomogr.* **11**, 332–337 (2017).
17. S. Lerakis, S. S. Hayek, P. S. Douglas, Paravalvular aortic leak after transcatheter aortic valve replacement: Current knowledge. *Circulation* **127**, 397–407 (2013).
18. J.-M. Sinning, C. Hammerstingl, M. Vasa-Nicotera, V. Adenauer, S. J. L. Cachiguango, A.-C. Scheer, S. Hausen, A. Sedaghat, A. Ghanem, C. Müller, E. Grube, G. Nickenig, N. Werner, Aortic regurgitation index defines severity of peri-prosthetic regurgitation and predicts outcome in patients after transcatheter aortic valve implantation. *J. Am. Coll. Cardiol.* **59**, 1134–1141 (2012).
19. K. Qiu, G. Haghiashtiani, M. C. McAlpine, 3D printed organ models for surgical applications. *Annu. Rev. Anal. Chem.* **11**, 287–306 (2018).
20. M. Vukicevic, B. Mosadegh, J. K. Min, S. H. Little, Cardiac 3D printing and its future directions. *JACC Cardiovasc. Imaging* **10**, 171–184 (2017).
21. M. Vukicevic, D. P. Vekilov, J. K. Grande-Allen, S. H. Little, Patient-specific 3D valve modeling for structural intervention. *Struct. Heart* **1**, 236–248 (2017).

22. A. Hosny, J. D. Dilley, T. Kelil, M. Mathur, M. N. Dean, J. C. Weaver, B. Ripley, Pre-procedural fit-testing of TAVR valves using parametric modeling and 3D printing. *J. Cardiovasc. Comput. Tomogr.* **13**, 21–30 (2019).
23. Z. Qian, K. Wang, S. Liu, X. Zhou, V. Rajagopal, C. Meduri, J. R. Kauten, Y.-H. Chang, C. Wu, C. Zhang, B. Wang, M. A. Vannan, Quantitative prediction of paravalvular leak in transcatheter aortic valve replacement based on tissue-mimicking 3D printing. *JACC Cardiovasc. Imaging* **10**, 719–731 (2017).
24. D. Maragiannis, M. S. Jackson, S. R. Igo, R. C. Schutt, P. Connell, J. Grande-Allen, C. M. Barker, S. M. Chang, M. J. Reardon, W. A. Zoghbi, S. H. Little, Replicating patient-specific severe aortic valve stenosis with functional 3D modeling. *Circ. Cardiovasc. Imaging* **8**, e003626 (2015).
25. B. Ripley, T. Kelil, M. K. Cheezum, A. Goncalves, M. F. Di Carli, F. J. Rybicki, M. Steigner, D. Mitsouras, R. Blankstein, 3D printing based on cardiac CT assists anatomic visualization prior to transcatheter aortic valve replacement. *J. Cardiovasc. Comput. Tomogr.* **10**, 28–36 (2016).
26. R. E. Clark, Stress-strain characteristics of fresh and frozen human aortic and mitral leaflets and chordae tendineae. Implications for clinical use. *J. Thorac. Cardiovasc. Surg.* **66**, 202–208 (1973).
27. K. Qiu, Z. Zhao, G. Haghiashtiani, S.-Z. Guo, M. He, R. Su, Z. Zhu, D. B. Bhuiyan, P. Murugan, F. Meng, S. H. Park, C.-C. Chu, B. M. Ogle, D. A. Saltzman, B. R. Konety, R. M. Sweet, M. C. McAlpine, 3D printed organ models with physical properties of tissue and integrated sensors. *Adv. Mater. Technol.* **3**, 1700235 (2018).
28. A. Hasan, K. Ragaert, W. Swieszkowski, Š. Selimović, A. Paul, G. Camci-Unal, M. R. Mofrad, A. Khademhosseini, Biomechanical properties of native and tissue engineered heart valve constructs. *J. Biomech.* **47**, 1949–1963 (2014).
29. G. A. Holzapfel, Biomechanics of soft tissue, in *The Handbook of Materials Behavior Models*, J. Lemaitre ed. (2001), vol. 3, pp. 1057–1071.
30. S. Ramadan, N. Paul, H. E. Naguib, Standardized static and dynamic evaluation of myocardial tissue properties. *Biomed. Mater.* **12**, 025013 (2017).
31. B. Wang, A. Borazjani, M. Tahai, A. L. de Jongh Curry, D. T. Simionescu, J. Guan, F. To, S. H. Elder, J. Liao, Fabrication of cardiac patch with decellularized porcine myocardial scaffold and bone marrow mononuclear cells. *J. Biomed. Mater. Res. A* **94**, 1100–1110 (2010).
32. K. J. Grande-Allen, R. P. Cochran, P. G. Reinhall, K. S. Kunzelman, Mechanisms of aortic valve incompetence: Finite-element modeling of Marfan syndrome. *J. Thorac. Cardiovasc. Surg.* **122**, 946–954 (2001).
33. P. S. Robinson, S. L. Johnson, M. C. Evans, V. H. Barocas, R. T. Tranquillo, Functional tissue-engineered valves from cell-remodeled fibrin with commissural alignment of cell-produced collagen. *Tissue Eng. Part A* **14**, 83–95 (2008).
34. A. S. Kamba, M. Ismail, T. A. T. Ibrahim, Z. A. B. Zakaria, Synthesis and characterisation of calcium carbonate aragonite nanocrystals from cockle shell powder (Anadara granosa). *J. Nanomater.* **2013**, 398357 (2013).
35. A. Hamdan, V. Guetta, E. Konen, O. Goitein, A. Segev, E. Raanani, D. Spiegelstein, I. Hay, E. Di Segni, M. Eldar, E. Schwammenthal, Deformation dynamics and mechanical properties of the aortic annulus by 4-dimensional computed tomography: Insights into the functional anatomy of the aortic valve complex and implications for transcatheter aortic valve therapy. *J. Am. Coll. Cardiol.* **59**, 119–127 (2012).
36. J. T. Muth, D. M. Vogt, R. L. Truby, Y. Mengüç, D. B. Kolesky, R. J. Wood, J. A. Lewis, Embedded 3D printing of strain sensors within highly stretchable elastomers. *Adv. Mater.* **26**, 6307–6312 (2014).
37. W. Shui, M. Zhou, S. Chen, Z. Pan, Q. Deng, Y. Yao, H. Pan, T. He, X. Wang, The production of digital and printed resources from multiple modalities using visualization and three-dimensional printing techniques. *Int. J. Comput. Assist. Radiol. Surg.* **12**, 13–23 (2017).
38. W. M. Yarbrough, R. Mukherjee, J. S. Ikonomidis, M. R. Zile, F. G. Spinale, Myocardial remodeling with aortic stenosis and after aortic valve replacement: Mechanisms and future prognostic implications. *J. Thorac. Cardiovasc. Surg.* **143**, 656–664 (2012).
39. P. R. Vijayaratnam, C. C. O'Brien, J. A. Reizes, T. J. Barber, E. R. Edelman, The impact of blood rheology on drug transport in stented arteries: Steady simulations. *PLOS ONE* **10**, e0128178 (2015).
40. M. Briand, J. G. Dumesnil, L. Kadem, A. G. Tongue, R. Rieu, D. Garcia, P. Pibarot, Reduced systemic arterial compliance impacts significantly on left ventricular afterload and function in aortic stenosis: Implications for diagnosis and treatment. *J. Am. Coll. Cardiol.* **46**, 291–298 (2005).
41. T. G. Papaioannou, A. D. Protogerou, N. Stergiopulos, O. Vardoulis, C. Stefanadis, M. Safar, J. Blacher, Total arterial compliance estimated by a novel method and all-cause mortality in the elderly: The PROTEGER study. *Age* **36**, 9661 (2014).
42. D. Chemla, J.-L. Hébert, C. Coirault, K. Zamani, I. Suard, P. Colin, Y. Lecarpentier, Total arterial compliance estimated by stroke volume-to-aortic pulse pressure ratio in humans. *Am. J. Physiol.* **274**, H500–H505 (1998).
43. M. Roşca, J. Magne, A. Călin, B. A. Popescu, L. A. Piérard, P. Lancellotti, Impact of aortic stiffness on left ventricular function and B-type natriuretic peptide release in severe aortic stenosis. *Eur. J. Echocardiogr.* **12**, 850–856 (2011).
44. S. G. Yazdi, P. Geoghegan, P. Docherty, M. Jermy, A. Khanafer, A review of arterial phantom fabrication methods for flow measurement using PIV techniques. *Ann. Biomed. Eng.* **46**, 1697–1721 (2018).
45. H. Baumgartner, J. Hung, J. Bermejo, J. B. Chambers, A. Evangelista, B. P. Griffin, B. Iung, C. M. Otto, P. A. Pellikka, M. Quiñones, Echocardiographic assessment of valve stenosis: EAE/ASE recommendations for clinical practice. *J. Am. Soc. Echocardiogr.* **22**, 1–23 (2009).
46. B. A. Carabello, W. J. Paulus, Aortic stenosis. *Lancet* **373**, 956–966 (2009).
47. A.-H. Hakki, A. S. Iskandrian, C. E. Bemis, D. Kimbiris, G. S. Mintz, B. L. Segal, C. Brice, A simplified valve formula for the calculation of stenotic cardiac valve areas. *Circulation* **63**, 1050–1055 (1981).
48. Y. Zhang, H. Ihlen, S. Nitter-Hauge, Estimation of the peak-to-peak pressure gradient in aortic stenosis by Doppler echocardiography. *Int. J. Cardiol.* **10**, 197–212 (1986).
49. M. F. Eleid, A. K. Cabalka, J. F. Malouf, S. Sanon, D. J. Hagler, C. S. Rihal, Techniques and outcomes for the treatment of paravalvular leak. *Circ. Cardiovasc. Interv.* **8**, e001945 (2015).
50. G. Rocatello, N. El Faquir, O. de Backer, M. J. Swaans, A. Latib, L. Vicentini, P. Segers, M. De Beule, P. de Jaegere, P. Mortier, The impact of size and position of a mechanical expandable transcatheter aortic valve: Novel insights through computational modelling and simulation. *J. Cardiovasc. Transl. Res.* **12**, 435–446 (2019).
51. K. Wang, Y. Zhao, Y.-H. Chang, Z. Qian, C. Zhang, B. Wang, M. A. Vannan, M.-J. Wang, Controlling the mechanical behavior of dual-material 3D printed meta-materials for patient-specific tissue-mimicking phantoms. *Mater. Design* **90**, 704–712 (2016).
52. H. Sabbah, P. Stein, Effect of aortic stenosis on coronary flow dynamics: Studies in an in-vitro pulse duplicating system. *J. Biomech. Eng.* **104**, 221–225 (1982).

Acknowledgments: We thank the Visible Heart Laboratories of the University of Minnesota for providing the tissue samples, D. Giles from the UMN Polymer Characterization Facility for support of mechanical and rheological tests, N. Carter for suggestions for the sol-gel testing of the polymers, B. McHenry for insightful discussions about applications of the 3D printed aortic root models in TAVR, Z. Zhu for assistance with developing the custom MATLAB script for the multimaterial 3D printing process, and S. Kodandaramaiah and L. Ghanbari for assistance with 3D printing of the test bar used in the calibration of the sensors. The use of cadaver tissue specimens in this work does not fall under the requirements of human participants research; therefore, an IRB review was not required. The schematic in Fig. 1A is drawn based on a schematic of the heart by user azwer distributed under a Creative Commons Zero License (available at https://www.needpix.com/photo/1038210/heart-anatomy-circulatory-health-medical-human-organ-science-medicine), and a schematic of the electrical conduction system of the heart by user Madhero88 distributed under a CC BY-SA 3.0 license (available at https://commons.wikimedia.org/wiki/File:Electrical_conduction_system_of_the_heart.svg; link to the license: https://creativecommons.org/licenses/by-sa/3.0/deed.en). **Funding:** Research reported in this publication was supported by Medtronic plc, the MnDRIVE program at the University of Minnesota, and the National Institute of Biomedical Imaging and Bioengineering of the National Institutes of Health under award number DP2EB020537. The content is solely the responsibility of the authors and does not necessarily represent the official views of the National Institutes of Health. G.H. acknowledges support from the graduate school of the University of Minnesota (2017–2018 Interdisciplinary Doctoral Fellowship and 2018–2019 Doctoral Dissertation Fellowship). **Author contributions:** G.H., K.Q., and M.C.M. designed the research concept and experiments. G.H. and K.Q. performed all the experiments and analyzed the data. J.D.Z.S. and P.A.I. contributed to design and execution of in vitro hemodynamic studies. Z.J.F. contributed to processing of STL models for fabrication and preparation of the custom MATLAB script for generating the G-code for multimaterial 3D printing process and assisted in preliminary tissue characterization. P.N. and S.E.A. contributed to conceptualization of applications of the models for conduction disturbances, processed CT scans of patients to obtain the corresponding STL files, performed CT scans on the 3D printed models, and executed the implanted valve frame analysis. G.H. and K.Q. wrote and M.C.M. edited the manuscript with contributions from all the coauthors. **Competing interests:** M.C.M., K.Q., and G.H. are inventors on a pending U.S. patent application related to this work filed by the University of Minnesota (US16/162,627; filed 17 October 2018). M.C.M. has received research grants from Medtronic and Boston Scientific and is on the editorial board of Science Advances. P.A.I. has a research contract and education consultant arrangement with Medtronic. S.E.A., P.N., and J.D.Z.S. are current employees of Medtronic, and Z.J.F. is a former employee of Medtronic. The authors declare that they have no other competing interests. **Data and materials availability:** All data needed to evaluate the conclusions in the paper are present in the paper and/or the Supplementary Materials. Additional data related to this paper is available at the data repository for the University of Minnesota (https://doi.org/10.13020/xjv7-s394) and from the authors upon request.

Submitted 27 February 2020
Accepted 6 June 2020
Published 28 August 2020
10.1126/sciadv.abb4641

Citation: G. Haghiashtiani, K. Qiu, J. D. Zhingre Sanchez, Z. J. Fuenning, P. Nair, S. E. Ahlberg, P. A. Iaizzo, M. C. McAlpine, 3D printed patient-specific aortic root models with internal sensors for minimally invasive applications. *Sci. Adv.* **6**, eabb4641 (2020).